Simulation of Atmospheric Circulation during the GIMEX 91 Experiment Using a Meso-γ Primitive Equations Model

HUBERT GALLÉE AND OLIVIER FONTAINE DE GHÉLIN

Institut d'Astronomie et de Géophysique Georges Lemaître, Université Catholique de Louvain, Louvain-la-Neuve, Belgium

MICHIEL R. VAN DEN BROEKE

Institute for Marine and Atmospheric Research, Utrecht University, Utrecht, the Netherlands

(Manuscript received 23 June 1994, in final form 15 May 1995)

ABSTRACT

A meso-γ-scale atmospheric model has been used to simulate atmospheric circulations observed during the Greenland Ice Margin EXperiment (GIMEX). The simulations shown here are two-dimensional and cover the 12–13 July 1991 period, a typical summer situation in this area. The synoptic-scale wind forcing is included. The tundra topography is assumed to be either flat, or averaged over a 50-km-wide cross section centered on the GIMEX transect. Simulated wind, temperature, humidity, and turbulent fluxes compare reasonably well with available observations. The simulated heat used to melt snow or ice is also shown. The sensitivity of the model results to the synoptic-scale wind forcing is significant. The impact of a tundra much warmer than the ocean on the ice sheet melting is discussed. It is found that weak easterly synoptic-scale winds are able to overwhelm this impact, especially when the tundra is assumed to be flat.

1. Introduction

One problem to be addressed in climatic change studies is the possible partial melting of huge ice sheets such as those over Greenland and Antarctica.

Among the processes governing the evolution of these ice sheets, the snow/ice mass budget has to be considered as critical. Variations in the melting rate in particular are suspected to play the most important role in the ice sheet mass balance variations, at least at the geological timescale (e.g., Gallée et al. 1992).

Moreover, a close link exists between the snow/ice surface energy balance and the melting (e.g., Ambach 1985), so that a good understanding of the processes responsible for the energy exchanges between the ice sheet and the atmosphere is necessary. A detailed ice sheet surface energy balance will certainly include the representation of the absorbed solar heat flux, the longwave radiation, the turbulent sensible and latent heat fluxes.

While variations in the absorbed fraction of the solar heat flux depend mainly on the surface albedo variations, which seem the most important process at timescales equal or larger than one season (e.g., Gallée et al. 1992), the turbulent heat fluxes play a significant role in coupling the atmosphere to the surface at shorter timescales. These fluxes are particularly large over the steep slopes of the ice sheets, generally in relation to katabatic wind (Lliboutry 1965). The width of the Greenland ice sheet ablation zone is typically a few tens of kilometers and includes the steepest slopes. Consequently, a detailed study of the ice sheet surface energy balance and melting would require an explicit representation of atmospheric processes having a horizontal length scale of 5–10 km. In the atmosphere, such horizontal length scale is classified as a meso-γ scale. Indeed, meso-γ-scale atmospheric processes are characterized by horizontal length scales ranging between 2 and 20 km (see, e.g., Stull 1993).

This stresses the importance of meso-γ-scale atmospheric modeling over the ice sheets. Such models may be validated using well-documented field experiments covering the ice sheet ablation zone. In turn, field experiments may be completed by simulations performed with them. An application of a validated meso-γ scale atmospheric models is to provide a link between the observations and the General Circulation Models (GCMs), even those which in the future will include an explicit representation of processes having an horizontal length scale as small as 50 km. In general, the ice sheet ablation zone should be considered as a subgrid-scale feature in these models and parameterized. To refine the climatology of a particular region, another

Corresponding author address: Dr. Hubert Gallée, Institut d'Astronomie et de Géophysique Georges Lemaître (Unité Astr), Université Catholique de Louvain, 2 Chemin du Cyclotron, B-1348 Louvain-la-Neuve, Belgium.
E-mail: gallee@astr.ucl.ac.be

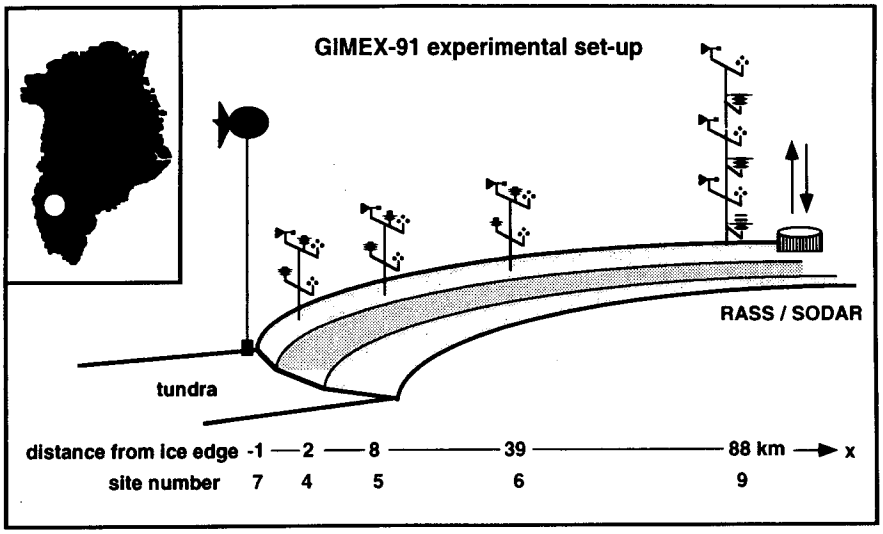

FIG. 1. Locations of five different sites used in the present study on a transect perpendicular to the ice edge.

possible application is the nesting into GCMs of meso-γ-scale atmospheric models properly designed for this task.

As shown by Oerlemans (1991), the western part of the Greenland ice sheet between 65°N and 70°N, is dry and warm. The equilibrium line in this region is significantly higher than elsewhere over the Greenland ice sheet. Implications for a climate change could be important. A modeling study (Letréguilly et al. 1991) has shown that this region may have been marked by an extensive melting during the isotopic stages 5e (130 kiloyears Before Present—kyr BP) and 5c (100 kyr BP). Furthermore, possible future greenhouse warming could also cause an extensive melting of the Greenland ice sheet in this region (Huybrechts et al. 1991).

The Greenland Ice Margin EXperiment (GIMEX), performed during the summer seasons of 1990 and 1991 in this region of Greenland provides a good database for testing mesoscale models. Until GIMEX, detailed meteorological measurements on Greenland have been limited to single locations (Ambach 1977a,b; Ohmura et al. 1992). The GIMEX experiments provide data with some (although still limited) horizontal resolution by the use of several independent masts, set up in an array along the ice sheet profile. This enables mesoscale modelers to check the performance of their models in order to make the step toward suitable boundary-layer parameterizations for GCMs over Greenland. The first results of GIMEX and other recent work concerning the Greenland ice sheet are collected and published in a special issue of *Global and Planetary Change* (No. 9, 1994).

The aim of this paper is to validate a meso-γ-scale atmospheric model for a GIMEX situation representative of average conditions during the melting period. For such condition, the synoptic-scale wind forcing has an easterly component most of the time. It will be included since it is typical for this part of Greenland (van den Broeke et al. 1994) and could play an important role in the katabatic wind behavior (e.g., Murphy and Simmonds 1993). Since we are dealing mainly with the influence of the turbulent energy fluxes on the ice sheet mass balance, we will restrict ourselves to a timescale comparable to the daily cycle. This will exclude the study of important processes such as those governing the snow albedo variations.

The remainder of this paper will be divided into five parts. In section 2, more details will be given on the field experiment itself. In section 3, a short model description will be provided. In section 4, the standard simulation results will be analyzed and compared with the available observations. Model sensitivity to the prescribed tundra topography and to the inclusion of the synoptic-scale forcing will be explored in section 5. Finally, conclusions will be given in section 6.

2. The GIMEX experiment

The GIMEX data were obtained in the western part of Greenland at a latitude of 67°N along a line approximately perpendicular to the ice sheet margin. Data are obtained from a series of masts and a captive balloon site as given by Oerlemans and Vugts (1993). The data from the two days of 12 and 13 July are particularly interesting because of the rather calm and stationary large-scale weather, with few clouds.

The general setup of the experiment in 1991 is given in Fig. 1. A total of seven unmanned masts was operated by Utrecht University and the Free University of

Amsterdam, the sites being numbered according to Fig. 1. At all sites, temperature and wind speed were measured at two levels or more, thus enabling the calculation of turbulent fluxes with Monin–Obukhov similarity theory, using hourly mean values of the profiles. Relative humidity profiles were measured at sites 7, 4, and 9 and used for the calculation of latent heat fluxes. Flux profile relations were used as presented by Duynkerke and van den Broeke (1994). All variables were sampled at 2-min intervals and converted into hourly mean values. This experimental setup has been used successfully on Alpine glaciers and also in Antarctica. The masts rest freely on the surface and melt down with the ice (the surface at site 4 lowered 2 meters during the experiment owing to ice ablation). Leaning of the masts was less than 5°. Data from all masts were transmitted by telemetry to the base camp. The total measuring period spanned 52 days in 1991, of which in this paper a case study is made of two days: 12 and 13 July 1991.

Since the main goal of the present study is an accurate simulation of the surface energy balance, we will concentrate on the surface observations at ice sites 4, 6, and 9 and the tundra site 7. Site 9 is estimated to be situated close to the mass-balance equilibrium line. Characteristic for the expedition area (just above the Arctic Circle at 67°N) is a 150-km wide strip of tundra, that allows for the highest mean summer temperatures in Greenland, exceeding +10°C (Ohmura 1987). Although the coastal areas experience persistent fog during the summer, the expedition area has a very dry and sunny climate. The general atmospheric circulation during the two day period under consideration is characterized by very small pressure gradients over West Greenland, resulting in a weak off-ice directed geostrophic flow over the expedition area. Cloud cover for both days is 1/8 or less. The maximum temperature at the airport of Søndre Strømfjord (25 km away from the ice edge) is +20°C for both days. This weather type is typical for this part of Greenland during summer. Meteorological conditions during these days are, therefore, expected to be representative for average summer conditions (van den Broeke et al. 1994).

The low tundra albedo of 0.2 and the very dry soil force a strong upward-directed sensible heat flux over tundra during sunny weather, while the sensible heat flux is downward directed over the melting ice (mainly due to the fixed surface temperature of the melting ice, see Duynkerke and van den Broeke 1994). As a consequence, very persistent katabatic winds dominate the stable surface layer of the ablation zone, while daytime conditions over the tundra are convective. The strong horizontal temperature difference between the boundary layer air over the tundra and over the ice (in the order of 10 K km^{-1}) further accelerates the air over the first ten kilometers of the ablation zone at day time, as has been described by van den Broeke et al. (1994). During the short night the opposite happens and the formation of a very stable boundary layer over the tundra decelerates the katabatic flow over the nearby ice. Further on the ice this influence of the tundra becomes weaker, and the daily cycle of the katabatic wind is reversed: maximum at night and minimum during the day, analogous to antarctic katabatic winds (Kodama et al. 1989).

The width of the ablation zone probably exceeds 100 km during the period under consideration, since strong melt was observed at site 9, 88 km away from the edge. A very interesting feature along the profile is the dip in surface albedo at site 6, probably caused by inefficient meltwater run off (Van de Wal and Russell 1994). Surface reflectivity at sites 4 and 5 remains constant at 0.55 throughout the season. At site 6, however, a marked decrease starts in July and results in very low values of 0.3 at the end of the season. Satellite observations confirm the existence of a zone of low reflectivity in the ablation zone which is several tens of kilometers wide, running for hundreds of kilometers south–north along the ice edge. This particular albedo profile has been used in the initialization of the model. Another important surface parameter, the aerodynamic roughness length z_0, also showed large variations along the profile. Values for z_0 published by Duynkerke and van den Broeke (1994) are used for the present runs and also held constant in time. Routinely measured background temperatures from the coastal weather station at Egedesminde (some 250 km to the north) are used for the initialization of background temperature and specific humidity.

3. The model

The atmospheric model (referred to hereafter as MAR[1]) is that of Gallée and Schayes (1994). It is a meso-γ-scale hydrostatic primitive equation model in which the vertical coordinate is the normalized pressure $\sigma = (p - p_t/p_s - p_t)$ (p_t = const, p_s and p being the model top pressure, the surface pressure, and the pressure, respectively). The full continuity equation is taken into account. The model is extensively described in Gallée and Schayes (1994) and is used here with the following modifications:

- Only the subgrid-scale fluxes on the σ surfaces and the vertical turbulent fluxes are taken into account, excluding the correction terms. This is justified by the fact that the correction terms contribution is negligible in katabatic winds simulations (Gallée and Schayes 1994; Gallée et al. 1993).
- Except in the surface layer, the vertical subgrid-scale fluxes are treated using the E-ϵ model of turbulence (Duynkerke 1988), allowing to represent the turbulent mixing length as a function of the local flow

[1] MAR: Modèle Atmosphérique Régional.

characteristics. This is important because of the complex structure of the katabatic layer (Pettré and André 1991; Gallée and Schayes 1992).

- To represent the vertical subgrid-scale fluxes in the surface layer, the formulation of Duynkerke (1991) and Duynkerke and van den Broeke (1994) is used.
- The Deardorff (1978) soil model has been adapted to the GIMEX situation. Over the tundra, the soil thermal conductivity is 0.65 W m^{-1} K^{-1}. Over the ice sheet, the snow/ice density is parameterized as in Meesters et al. (1994), while the snow heat conduction coefficient is parameterized as in Yen (1981). When the ice sheet surface temperature exceeds 273.15 K, it is reset to 273.15 K, and a resulting meltwater flux is computed.
- The lateral boundary conditions are modified to take into account the synoptic scale, and involve "relaxing" the model-predicted variables toward the large-scale analysis (Anthes et al. 1989).
- To take into account a nonzero geostrophic forcing, the synoptic-scale flow is included by constraining its potential vorticity to remain constant. This is done, in particular, to define the geostrophic wind, the initial wind, and to update the lateral boundary conditions for the wind at each time step. Details are given in the appendix. The model sensitivity to the constant potential vorticity constraint will be discussed in section 5.

4. Standard simulation

a. Initialization

The simulations shown here are done with the two-dimensional model version, with the model domain perpendicular to the ice margin. This is a reasonable assumption since the ice sheet topography and albedo may be assumed as two-dimensional in the GIMEX area. Another reason is that the two-dimensional version of the model is not CPU expensive, so that a lot of sensitivity experiments may be done with the model.

The horizontal grid size is 5 km and there are 17 nonuniformly distributed vertical levels (i.e., 15 365, 12 224, 9386, 6862, 4717, 3028, 1819, 1032, 561, 295, 153, 78, 39, 20, 10, 5, and 2.50 m).

Initial air temperature and humidity are taken from the Egedesminde sounding on 13 July 1991 at 0000 UTC. The synoptic-scale forcing is that of the 700-hPa level in the Egedesminde sounding and varies in time. The synoptic-scale wind speeds (m s^{-1}) V_L and directions dd_L at Egedesminde are $V_L e^{idd_L} = 4e^{i105°}$, $4e^{i130°}$, $3e^{i95°}$, $4e^{i55°}$, $4e^{i355°}$, respectively on 12 July at 0000 UTC, 1200 UTC; on 13 July at 0000 UTC, 1200 UTC; and on 14 July at 0000 UTC. Interpolation is performed between at each time step.

The ice sheet topography is prescribed using an idealized profile taken from Oerlemans and van der Veen (1984):

$$h_s = \left(\frac{2\tau_0 x}{\rho g}\right)^{1/2}, \qquad (1)$$

where τ_0 represents the ice yield stress (100 kPa) and ρ the ice density (900 kg m^{-3}). Although the ice sheet topography may be assumed as two-dimensional in the GIMEX area, this assumption is rather crude for the hilly tundra. Several tests, including a three-dimensional test, have been made to determine the impact of a prescribed tundra topography on the simulated atmospheric circulation over the ice sheet. It is found that only the marginal area of the ice sheet is significantly affected by the choice of the tundra topography. This is a rather small part of the ice sheet domain. The reason is that the large-scale and katabatic circulations come from the ice sheet interior.

The best agreement between observations and simulation near the ice sheet margin is found when taking a tundra topography meridionally averaged along a 50-km wide cross section centered on the GIMEX transect. This topography will be referred to as the hilly tundra topography in the remaining of the paper. The agreement is poorer when assuming a flat tundra, and simulated wind speed differs from that of the previous simulation by up to roughly 20% in the ice sheet margin area. This indicates that the model results in the ice-sheet margin area have to be considered with caution. With a 150-m high flat tundra, the agreement is somewhat in between that obtained with the abovementioned assumptions.

Finally, the three-dimensional test does not reveal a significant improvement of the model results. This is due to the fact that topographic features such as f jords, which could play a significant role in the katabatic circulation over the tundra, are too small and are consequently crudely represented in the model. Because the present study is dealing mainly with the katabatic circulation over the ice sheet, the small improvements obtained in the three-dimensional test confirm that it is reasonable to use the two-dimensional version of the model.

The standard simulation will therefore be performed with the hilly tundra topography. More details about the model sensitivity to the prescribed tundra topography will be given in section 5. Note that the topography has been filtered in order to avoid the generation of 2 Δx waves.

Sea surface temperature is fixed at the freezing point (271.2 K). Over the tundra and the ice sheet, the initial mean soil temperatures used in the Deardorff (1978) soil model are T_t = 289.2 K and T_i = 273.15 K, respectively. The initial soil surface temperature is that of the sounding, except over the ice sheet where it is not allowed to exceed 273.15 K. The surface albedo is prescribed and is taken from the GIMEX data. It equals 0.2 over the tundra. Over the ice sheet, it is equal to 0.55, 0.55, 0.35, 0.35, 0.50, 0.62, and 0.82, respectively, at 0, 10, 30, 50, 70, 90, and 235 km from the margin and is interpolated in between. The surface roughness length for momentum is also defined as found by Duynkerke and van den Broeke (1994). It is

divided by a factor of 10 for computing heat and humidity fluxes.

b. Model performance

In this section, we analyze in detail the results of the standard simulation. The simulation is started at 0000 LT on 12 July and is conducted over 48 h. Since roughly a 12-h time integration is needed before the katabatic wind is well established, only the results of the last 36-h time integration are shown. In Fig. 2, the circulation characteristics observed at mast 7 (base camp located on the tundra, 0.8 km from the ice sheet margin) are compared with the simulation at the first tundra grid point (starting from the ice sheet margin) for 12–13 July 1991. The agreement is rather good, except perhaps for the wind direction, which is simulated from the southeast, while the observations are marked by northeasterly winds. In fact, the observed winds are influenced by channeling of the cold air into the fjord, which is not represented in the two-dimensional topography.

In Fig. 3, the circulation characteristics observed at mast 4 (located on the ice sheet, 2.2 km far from the ice sheet margin) are compared with the simulation at the first ice sheet grid point (starting from the ice sheet margin) for 12–13 July 1991. The agreement is not as good than for mast 7, except for the wind direction. The simulation is more marked by the katabatic circulation than is found in the observations. This is reflected in the more relative constancy of the simulated wind speed and by the retardation of the wind speed minimum at night, as compared to the observations. As mentioned before, this could be due to the two-dimensional representation of the tundra topography. Another possible cause of this shortcoming could be an underestimation of the observed roughness length at mast 4.

As it is seen from Figs. 4 and 5, the agreement between observations and simulation is better for masts 6 and 9 (located over the ice sheet, respectively, 39 and 88 km far from the ice sheet margin) than for mast 4. Simulation and observations are comparable, except at mast 9 where the simulated latent heat flux is generally underestimated during daytime. Although the observed latent heat flux is not available for mast 6, it could be inferred that the simulated latent heat flux over the ice sheet increases from mast 4 to mast 9, as in the observations.

Over the ice sheet, the observed wind direction is SE. This behavior is also found in the simulation at masts 4, 6, and 9. It is also found that the simulated sensible heat flux is always downward, as in the observations.

To summarize the comparison between the simulation and the observations, the heat amount available for snow/ice melting (i.e., the energy equivalent of the reduction of the snow temperature to 0°C, see section 3) is shown in Fig. 6 for the second day of integration (13 July) as a function of the distance to the ice sheet margin. At masts 4 and 9, the difference with the melted ice amount per day computed from the observed surface heat fluxes remains within 10%.

The details of the simulated surface energy budget averaged over the same day are also shown (see Table 1). It is found that the absorbed solar heat flux dominates everywhere. Over the ice sheet, it is the most important at mast 6, because of the low surface albedo there. The net infrared heat losses increase with the altitude of the ice sheet surface because of a decrease in the downward infrared heat flux. Simulated latent heat fluxes are of secondary importance.

The sensible turbulent heat flux absorbed by the ice sheet surface is an important component of the surface energy budget. It amounts to roughly 40% of the absorbed solar heat flux at masts 6 and 9 and is larger than roughly 50% at mast 4, but this last value could be overestimated, because of the excessive wind speed simulated at mast 4. In general, the sensible heat flux increases downslope between mast 9 and the ice sheet margin area. This results from an increase of the wind speed and of the vertical potential temperature gradient between the surface and the katabatic layer. The main reason is that the snow/ice temperature may not be larger than the melting point. Observations have shown that the katabatic winds are very persistent over the ice sheet margin in the GIMEX area (van den Broeke et al. 1994). Consequently, the importance of the sensible heat fluxes in the surface energy budget reflects the influence of the katabatic winds on the Greenland ice sheet mass balance in this area.

c. Katabatic flow characteristics

Figures 7 and 8, show, respectively, the wind speed and the downslope wind component for the second day of integration (i.e., 13 July) at 1500 LT. Figures 9 and 10 show the potential temperature field for the second day of integration at 0300 LT and 1500 LT, respectively. It is seen that katabatic flow dominates over the ice sheet. For the highest surface elevations, the temperature inversion is stronger at 0300 LT. Near the ice sheet margin, the slopes are steeper and a well-marked temperature inversion is maintained even at 1500 LT. This results from the fact that the air mass is much warmer than the melting ice there, a situation different from what is found for Adélie Land (Antarctica), where anabatic flow may be observed during daytime over the steep coastal slopes.

At distances larger than 50 km, the wind speed (Fig. 7) increases downslope. This is due to the fact that the buoyancy force (i.e., slope inversion force, see Mahrt 1982) dominates. Between 150 km and 10 km far from the ice sheet margin, the height of the wind speed maximum is 75 m. This is typical of what is observed at site 9, 88 km far from the ice sheet margin (Oerlemans and Vugts 1993). The maximum wind speed is simu-

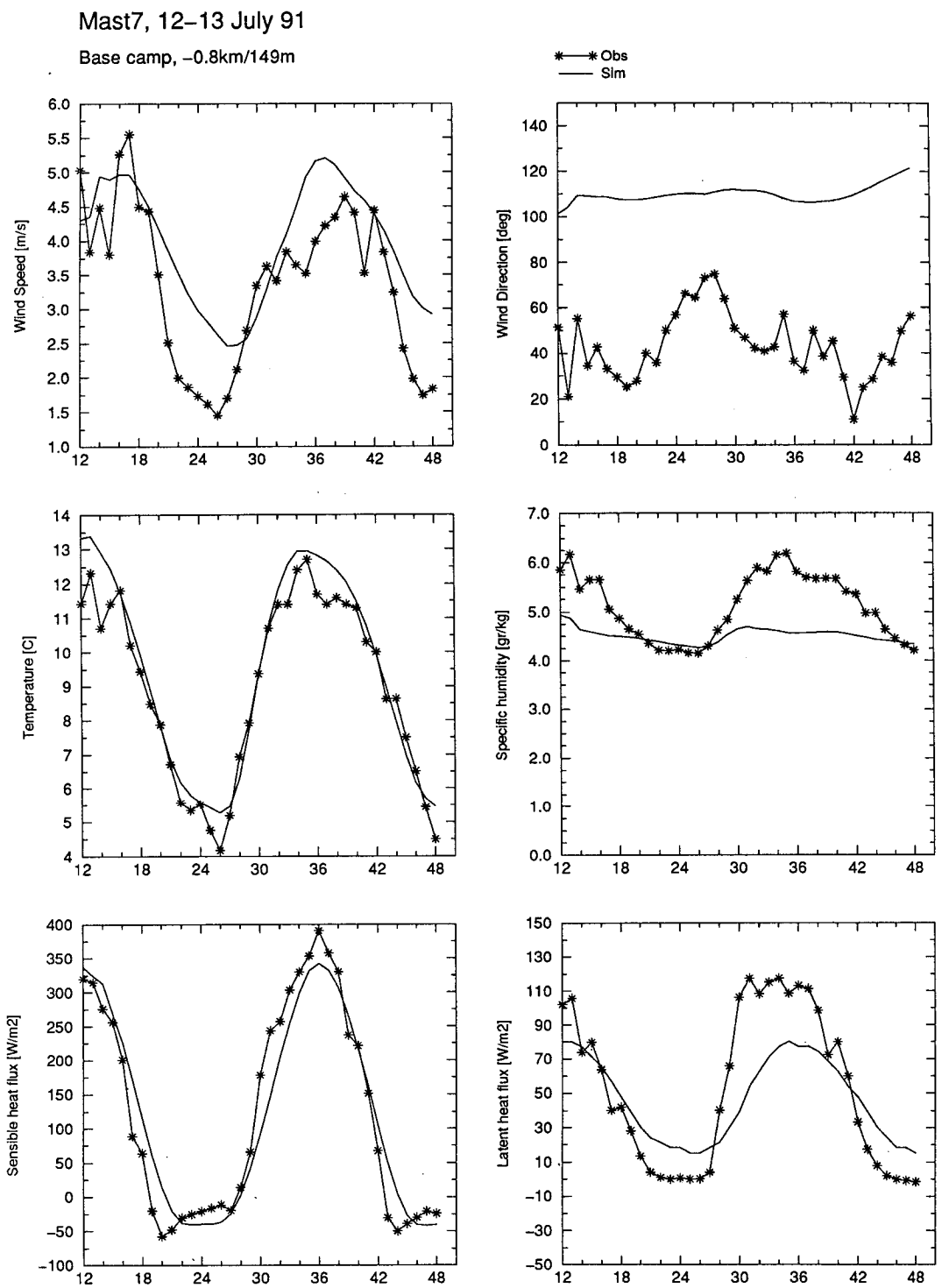

FIG. 2. Comparison between observations and the standard simulation for mast 7 (base camp, located on the tundra, 0.8 km from the ice sheet margin): (1) top left panel: wind speed 6 m above the surface (in m s^{-1}); (2) top right panel: wind direction (in degrees); (3) middle left panel: temperature 2 m above the surface (in K); (4) middle right panel: air specific humidity 2 m above the surface (in g kg^{-1}); (5) bottom left panel: sensible heat flux (in W m^{-2}—positive upward); (6) bottom right panel: latent heat flux (in W m^{-2}—positive upward). The observations are represented by the stars.

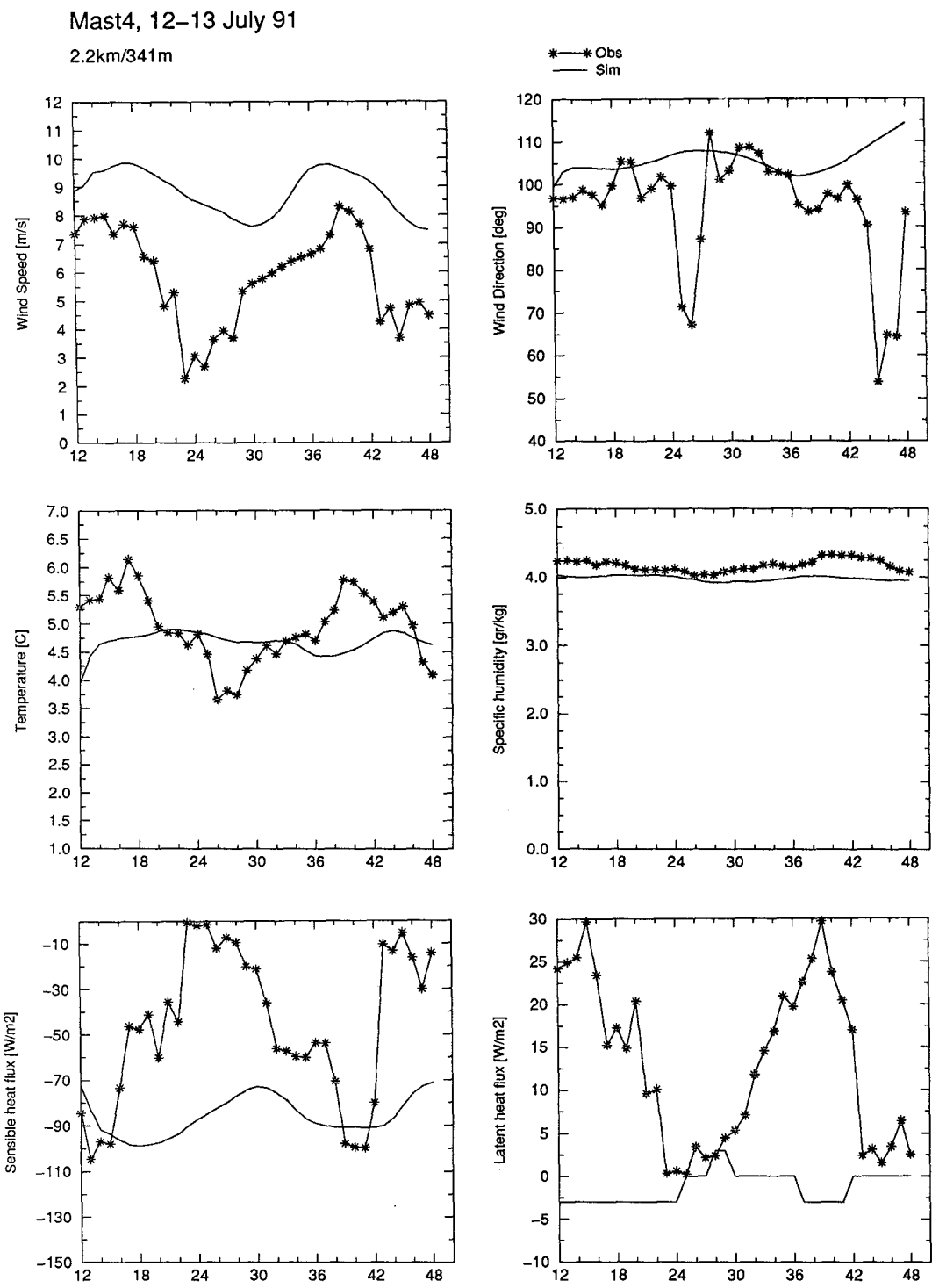

FIG. 3. Comparison between observations and the standard simulation for mast 4 (located on the ice sheet, 2.2 km from the ice sheet margin): (1) top left panel: wind speed 6 m above the surface (in m s^{-1}); (2) top right panel: wind direction (in degrees); (3) middle left panel: temperature 2 m above the surface (in K); (4) middle right panel: air specific humidity 2 m above the surface (in g kg^{-1}); (5) bottom left panel: sensible heat flux (in W m^{-2}—positive upward); (6) bottom right panel: latent heat flux (in W m^{-2}—positive upward). The observations are represented by the stars.

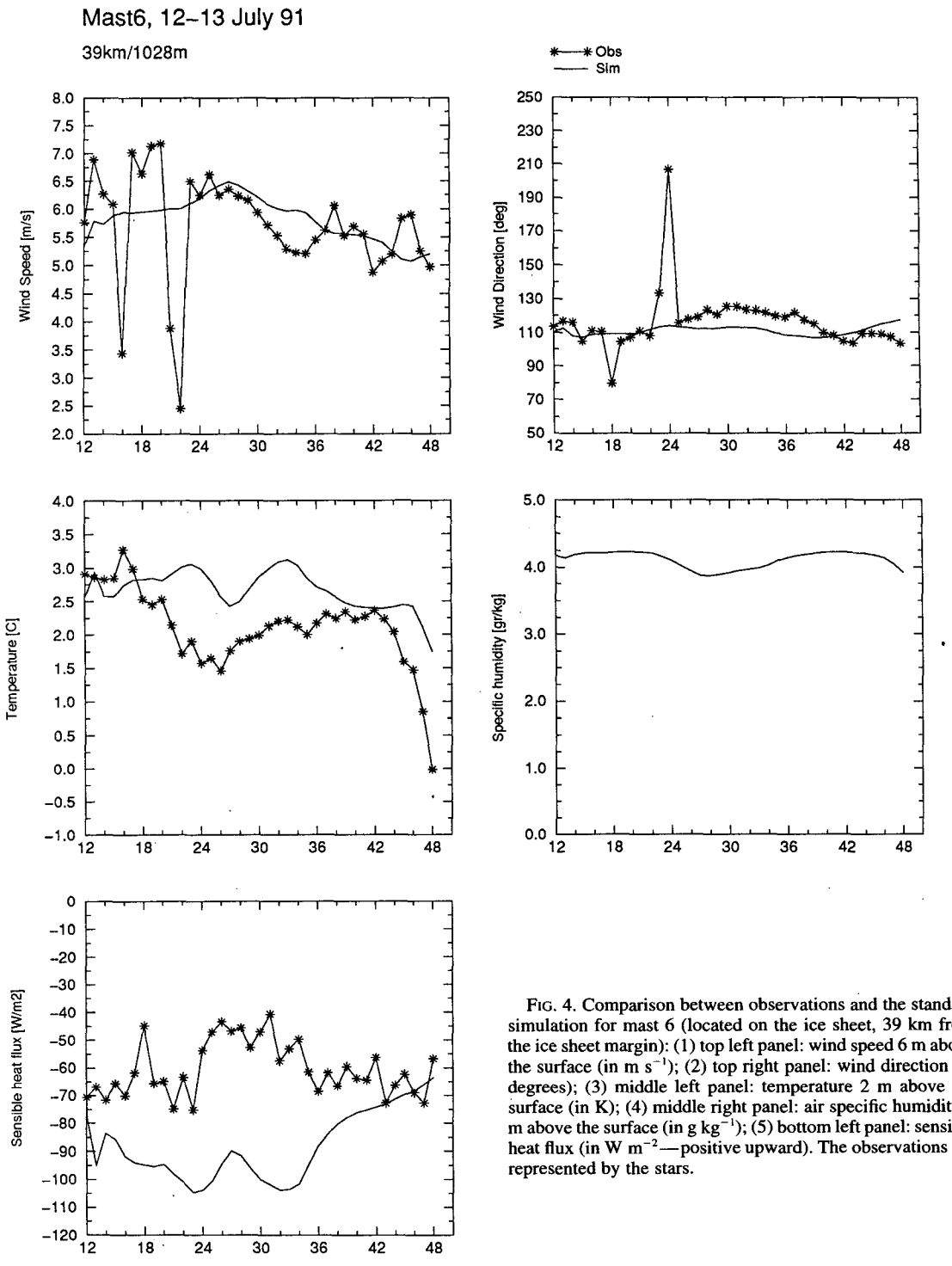

FIG. 4. Comparison between observations and the standard simulation for mast 6 (located on the ice sheet, 39 km from the ice sheet margin): (1) top left panel: wind speed 6 m above the surface (in m s^{-1}); (2) top right panel: wind direction (in degrees); (3) middle left panel: temperature 2 m above the surface (in K); (4) middle right panel: air specific humidity 2 m above the surface (in g kg^{-1}); (5) bottom left panel: sensible heat flux (in W m^{-2}—positive upward). The observations are represented by the stars.

lated roughly 50 km far from the ice sheet margin. Contrasting with the wind speed, the downslope wind component exhibits two local maxima. The largest one occurs over the steepest slopes and in lower model layers (Fig. 8). The increase of the downslope wind component contribution to the wind speed, where slopes increase, is a classical feature of katabatic flows. Another interesting feature found in Fig. 8 is that the downslope wind component becomes zero near the ice sheet margin, roughly 300 m above the surface. Keeping in mind

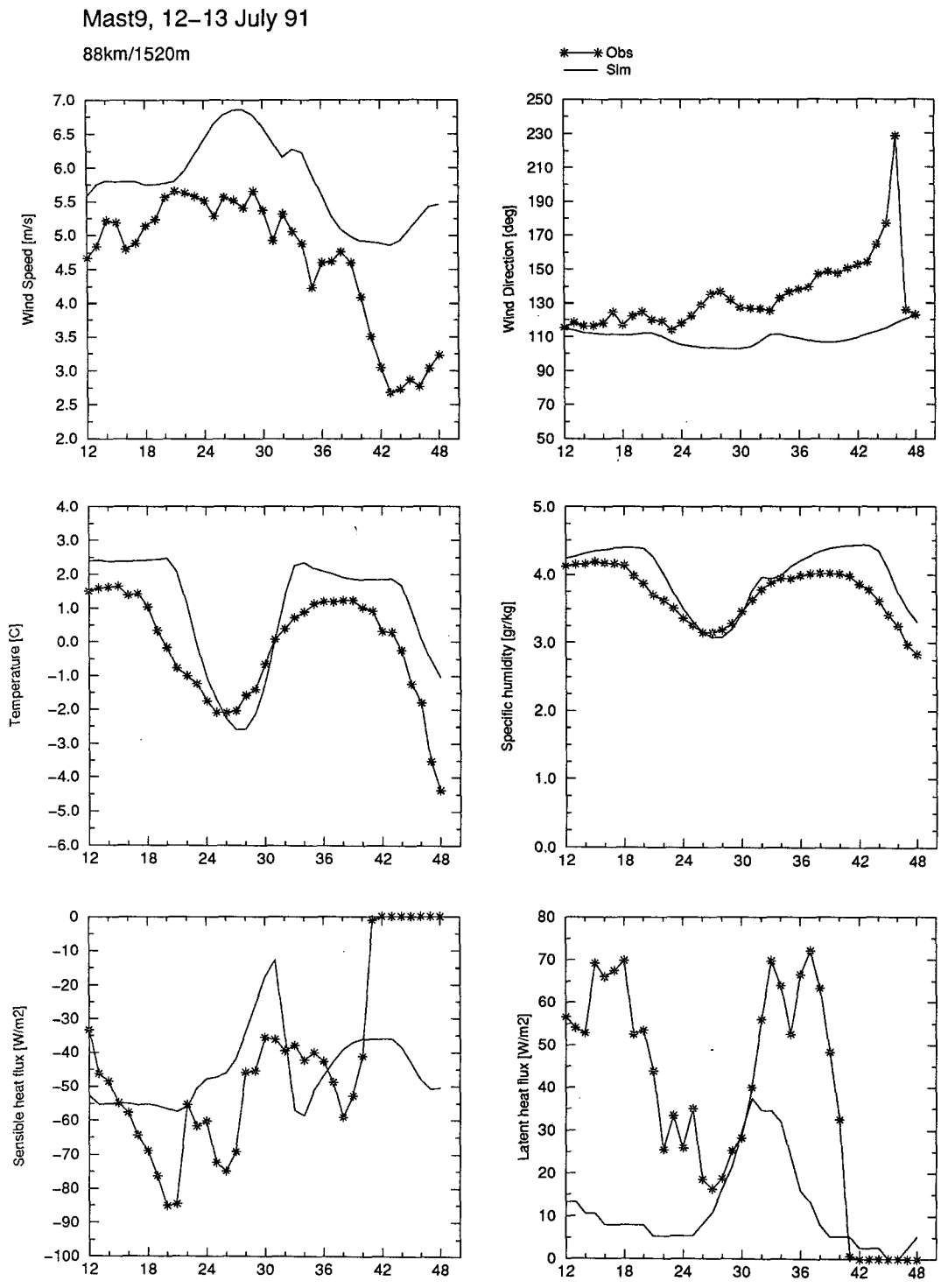

FIG. 5. Comparison between observations and the standard simulation for mast 9 (located on the ice sheet, 88 km from the ice sheet margin): (1) top left panel: wind speed 6 m above the surface (in m s^{-1}); (2) top right panel: wind direction (in degrees); (3) middle left panel: temperature 2 m above the surface (in K); (4) middle right panel: air specific humidity 2 m above the surface (in g kg^{-1}); (5) bottom left panel: sensible heat flux (in W m^{-2}—positive upward); (6) bottom right panel: latent heat flux (in W m^{-2}—positive upward). The observations are represented by the stars.

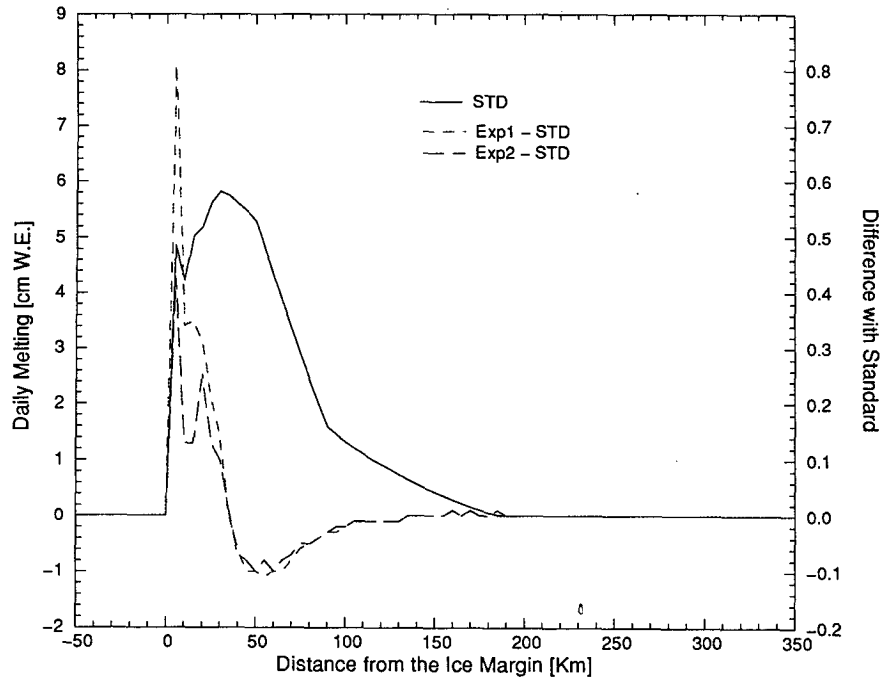

FIG. 6. Heat available for ice/snow melt (in cm WE day^{-1}) as a function of the distance to the ice sheet margin (in km), for the second simulated day (corresponding to 13 July 1991), and for the standard simulation (hilly tundra, solid line). Comparison between the standard and sensitivity experiments: dashed line: experiment 1 minus standard (the tundra is assumed to be 0 m high); axis line: experiment 2 minus standard (the tundra is assumed to be replaced by ocean).

that the geostrophic downslope wind component is roughly 3 m s^{-1} at this time, this means that a return flow is simulated aloft in this area.

The analysis of the potential temperature field (Figs. 9 and 10) reveals that over the steepest ice sheet slopes, the katabatic layer is fully developed. It consists, from the surface upward, of a thin cold-air surface layer, followed by a very stable inversion layer for which strength decreases downslope, a slightly unstable layer thickening downslope (in which $0 > \partial\theta/\partial z$

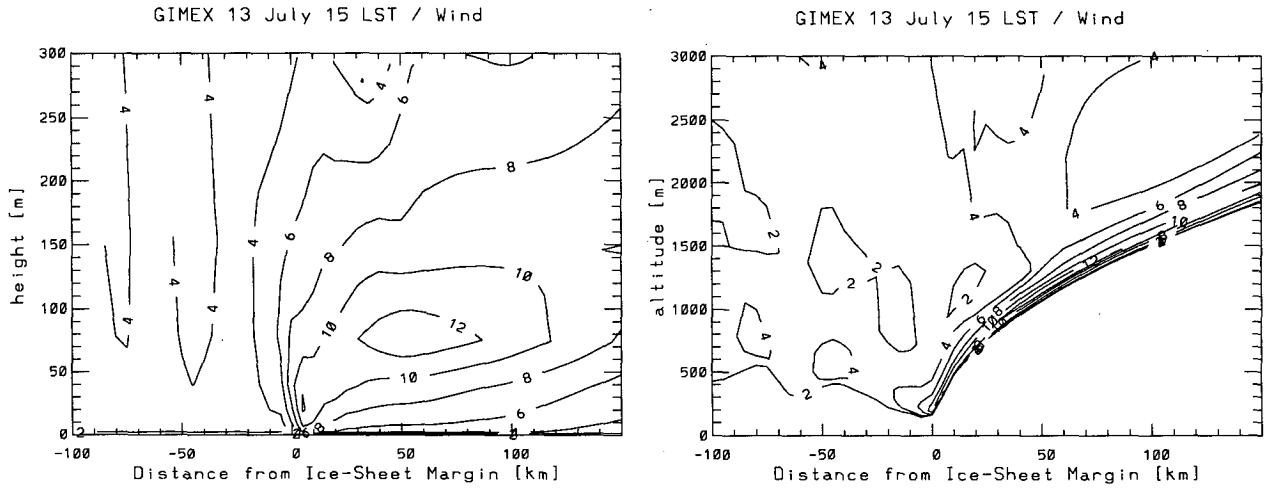

FIG. 7. The wind speed in the vertical plane of integration for the standard experiment, after 39-h time integration (i.e., on 13 July at 1500 LT), as a function of distance to the ice sheet margin (positive distances are on the ice sheet) and height above the surface (panel a) or altitude (panel b). Positive values indicate downslope wind and are represented by solid lines. Contour interval of 2 m s^{-1}.

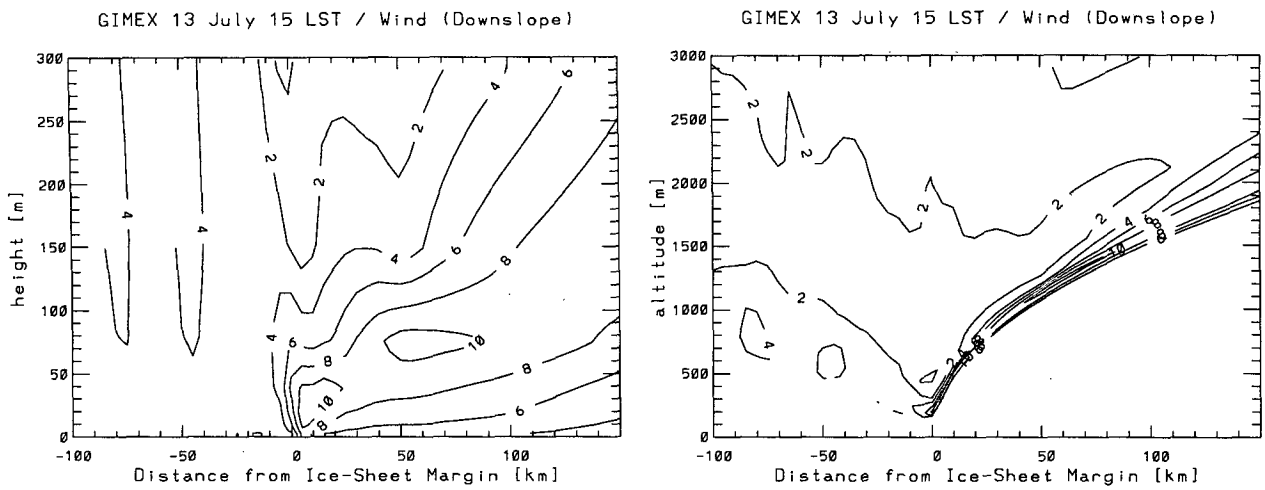

FIG. 8. The x (downslope) component of the wind field in the vertical plane of integration for the standard experiment, after 39-h time integration (i.e., on 13 July at 1500 LT), as a function of distance to the ice sheet margin (positive distances are on the ice sheet) and height above the surface (panel a) or altitude (panel b). Positive values indicate downslope wind and are represented by solid lines. Contour interval of 2 m s^{-1}. Note the 0 m s^{-1} contour simulated above the ice sheet margin (height above the surface: 300 m, altitude 500 m).

$> -1°C\ km^{-1}$), and a stable transition layer to the overlying free atmosphere. In this area, the apparent adiabatic nature of the katabatic flow, contrasting with the stable air mass stratification, especially at 0300 LT, seems to be the main cause of the unstable layer thickening; the stabilizing turbulent heat exchanges being relatively less important. For example, 5 km far from the ice sheet margin, the model simulates at 0300 LT and 1500 LT, respectively, a 150-m and 200-m deep unstable layer from roughly 100 m above the ice sheet surface. Over the tundra, the slope inversion force vanishes and the katabatic flow slows down. Consequently, the cold katabatic air is piling up, so that the stable inversion layer thickens and the unstable layer disappears. The piling up effect is well marked in the vertical wind speed component (not shown) and is responsible for the generation of a vertically propagating gravity wave. When assuming a flat tundra, the piling up effect is also significant but slightly less efficient (see section 5). Because the unstable layer is replaced by a colder stable layer over the tundra, an associated pressure gradient force (i.e., thermal wind force, see Mahrt 1982)

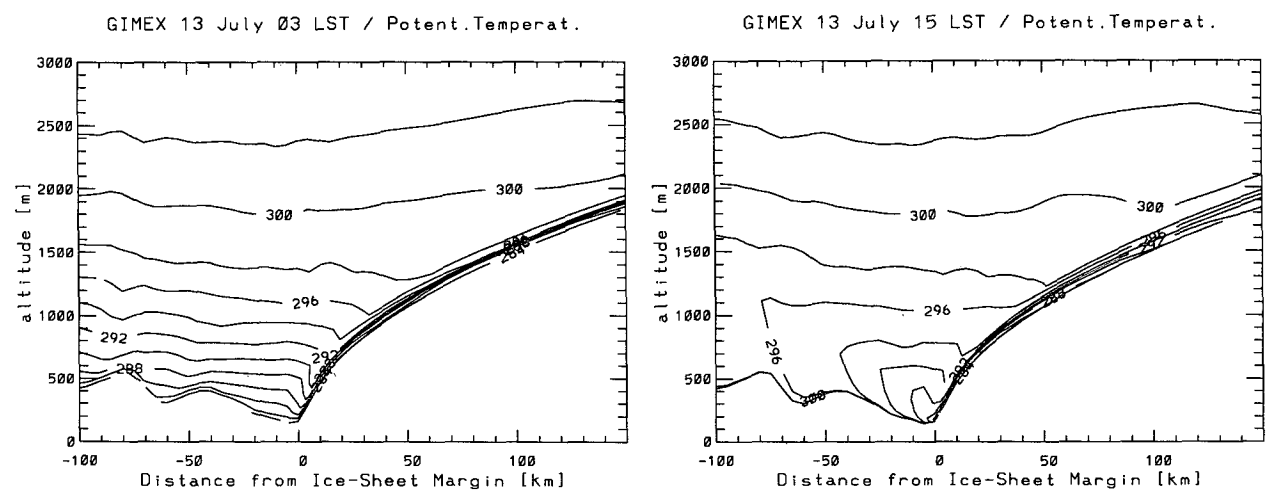

FIG. 9. The potential temperature in the vertical plane of integration for the standard experiment, after 27-h time integration (i.e., on 13 July at 0300 LT), as a function of distance to the ice sheet margin (positive distances are on the ice sheet) and altitude. Contour interval of 2 K.

FIG. 10. The potential temperature in the vertical plane of integration for the standard experiment, after 39-h time integration (i.e., on 13 July at 1500 LT), as a function of distance to the ice-sheet margin (positive distances are on the ice sheet) and altitude. Contour interval of 2 K.

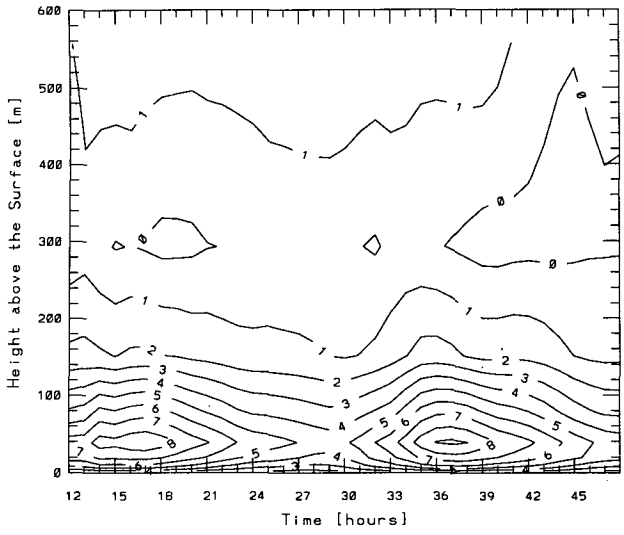

FIG. 11. Standard experiment: time–height cross section of the x (downslope) component of the wind field, for the last 36-h time integration of the 12–13 July 1991 period, at mast 7. Contour interval of 1 m s^{-1}.

results from density gradients along the x axis. It is directed from the tundra toward the ice sheet. This is why the model simulates a decrease of the wind speed in the upper part of the katabatic layer, 30 km upwind of the ice sheet margin. Nevertheless, the katabatic flow is not completely stopped since the slope inversion force still exists between the cold melting ice sheet and the overlaying warm air. Above the unstable layer, the impact of the slope inversion force is very small but a slight thermal wind force persists, perhaps due to the piling up of the katabatic air in the ice sheet margin area. It seems that the abovementioned return flow (Fig. 8) could be associated to this residual thermal wind force.

During daytime only, the simulated downslope wind speed component is maximum near the ice sheet margin. At mast 7 the wind speed simulation (Fig. 2) and the downslope wind component [Fig. 11, see also van den Broeke et al. (1994), their Fig. 8] also exhibit a maximum during daytime. One could explain the daily wind speed maximum at mast 7 by the persistence of the katabatic winds near the ice sheet margin and by an ice breeze effect. The ice breeze effect is due to the temperature gradient that is generated during daytime between the warm tundra and the cold ice sheet (e.g., van den Broeke et al. 1994). More generally, daytime over the tundra is marked by the development of a convective boundary layer roughly 1000 m thick. Indeed, the solar heat flux absorbed by the tundra surface is important during this period of the year.

As a consequence of the katabatic wind persistence and the ice breeze effect, katabatic wind circulation tends to penetrate over the tundra. In particular, the potential temperature time–height cross section [Fig. 12, see also van den Broeke et al. (1994), their Fig. 9] reveals maximum values in the potential temperature around 1200 LT, extending upward from 150 m above the surface. The near-neutral air stratification above 150 m at this time seems to be more related to the signature of a katabatic unstable layer than to a subsidence effect due to a pure ice breeze.

Despite the fact that the ice breeze effect is responsible for an increase of the simulated wind over the tundra during daytime, winds are generally weaker over the tundra than over the ice sheet.

During nighttime, the temperature difference between the tundra and the ice sheet decreases and even becomes reversed in observations, so that there is no ice breeze effect. Consequently, the cold katabatic air piling up effect plays a relatively increasing role in the atmospheric dynamics near the ice sheet margin. The associated thermal wind force causes a decrease of the simulated wind over the tundra while it is maintained over the ice sheet. This leads to a stronger transition in the atmospheric circulation between the ice sheet and the tundra, as it is also found in the observations.

5. Sensitivity experiments

In this section, the MAR sensitivity to the representation of the tundra and the synoptic-scale wind forcing will be discussed. The impact of the tundra heating on the ice sheet melting will also be shown. The experiments are summarized in Tables 2 and 3. and described in detail in the remainder of the section.

a. Sensitivity to the tundra topography representation

We will now analyze the model sensitivity to the representation of the tundra topography by assuming a

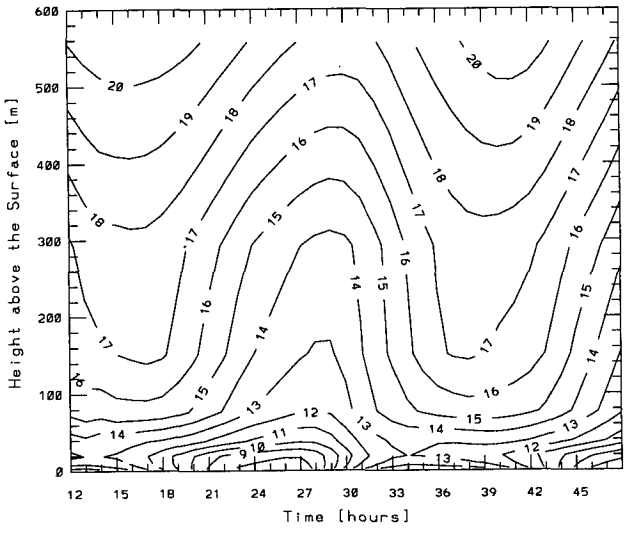

FIG. 12. Standard experiment: potential temperature time–height cross section, for the last 36-h time integration of the 12–13 July 1991 period, at mast 7. Contour interval of 1 K.

TABLE 1. Standard simulation along the GIMEX transect. Atmospheric heat fluxes (W m^{-2}) at the surface, and averaged over the 13 July 1991. Positive values refer to heat fluxes absorbed by the surface. The distance from the ice sheet margin (km) and the altitude (m) of the masts in the model are also included.

Mast	Distance	Altitude	Absorbed solar	Net infrared	Sensible	Latent
7	−2.5	160	248	−83	−121	−45
4	2.5	305	145	−39	83	0
6	37.5	950	209	−61	87	−18
9	87.5	1427	106	−71	40	−16

0-m-high flat tundra (experiment 1) and comparing the results to those obtained with the standard (in which the hilly tundra topography is taken). Note that for the three last tundra grid points (before the ice sheet margin) and the two first ice sheet grid points, the surface heights in experiment 1 are 0, 0, 84, 287, 468 m in place of 174, 142, 160, 305, 468 m in the standard, (giving at mast 4 a slope amounting to 4% and 3%, respectively). In Table 3, it is found that experiment 1 is very similar to the standard, except for mast 4, where the differences with the observations are generally larger for experiment 1. More precisely in Fig. 13, the circulation characteristics observed at mast 4 (located on the ice sheet, 2.2 km far from the ice sheet margin) are compared with the results of experiment 1 at the first ice sheet grid point (starting from the ice sheet margin) for 12–13 July 1991. The agreement is less good than for the standard, especially for the simulated wind speed, which is larger and exhibits a nonrealistic constancy. The larger simulated wind speeds at mast 4 in experiment 1 could be due partly to the larger prescribed ice sheet slope in this area (4%) than in the standard (3%). The sensible heat flux is also marked by a nonrealistic constancy, probably due to the nonrealistic wind speed constancy. Moreover, the simulated time–height cross section at mast 7 for the downslope wind speed component (not shown) is marked by a nonrealistic nighttime maximum. Nevertheless, a comparison of the simulated wind field at 0300 LT with that of the standard reveals small differences. Only a slight nighttime penetration of the katabatic flow over the tundra is found in the sensitivity experiment 1 while the discontinuity in the atmospheric circulation between the tundra and the ice sheet is maintained. In the sensitivity experiment 1, this is due to a slightly less efficient piling up of the cold dense katabatic air over the tundra. Although these model results must be considered with caution because of the three-dimensionality of the real tundra topography, the comparison between the standard and experiment 1 seems to confirm the occurrence of a piling up effect.

To assess the impact of the presence of a tundra much warmer than the ocean (hot tundra) on the model sensitivity, experiment 1 has been reconducted with tundra replaced by ocean (experiment 2, see Table 2). The main results are shown in Table 3. No sensitivity is found for the 0-m high flat topography assumption except perhaps at mast 4. Figure 6 shows the 13 July melting for the standard and the differences with that of experiments 1 and 2. It is found that these differences are large near the ice margin, amounting to 0.8-cm water equivalent (cm WE) for experiment 1. In this area, the larger melting in experiments 1 and 2 than in the standard is mainly due to the above-mentioned larger wind speed. It is also found that, in contrast to the standard and experiment 1, experiments 1 and 2 are very similar, except perhaps in the first 30 km over the ice sheet. This indicates the larger model sensitivity to the

TABLE 2. Simulations of the 12–13 July 1991 along the GIMEX transect. Description of the sensitivity experiments to the tundra representation and to the synoptic-scale forcing. The tundra topography is either averaged along a 50-km-wide cross section centered on the GIMEX transect (hilly tundra topography), either assumed to be flat, 0-m-high, referring to sea level. The subscript 0 refers to values at the sounding location. Here u_L and v_L are the synoptic-scale wind components. $E = (\zeta_L + f)/p_{*L}$, where ζ_L, f, and p_{*L} are, respectively, the relative vorticity, the Coriolis parameter, and the synoptic-scale pressure thickness $p_{sL} - p_t$, represents the potential vorticity of the synoptic-scale flow. When mentioned, the 700-hPa level of the Egedesminde sounding is included.

Exp.	Large-scale wind forcing	Wind initialization		Tundra representation	
		x component	y component	topography	surface
STD	Egedesminde	$p_{*L}u_L = p_{*,0}u_{L,0}$	$E = E_0$	Hilly	Tundra
1	Egedesminde	$p_{*L}u_L = p_{*,0}u_{L,0}$	$E = E_0$	0 m High	Tundra
2	Egedesminde	$p_{*L}u_L = p_{*,0}u_{L,0}$	$E = E_0$	0 m High	Ocean
3	Egedesminde	$p_{*L}u_L = p_{*,0}u_{L,0}$	$v_L = v_{L,0}$	Hilly	Tundra
4	0	$u_L = 0$	$v_L = 0$	Hilly	Tundra
5	0	$u_L = 0$	$v_L = 0$	0 m High	Tundra
6	0	$u_L = 0$	$v_L = 0$	0 m High	Ocean

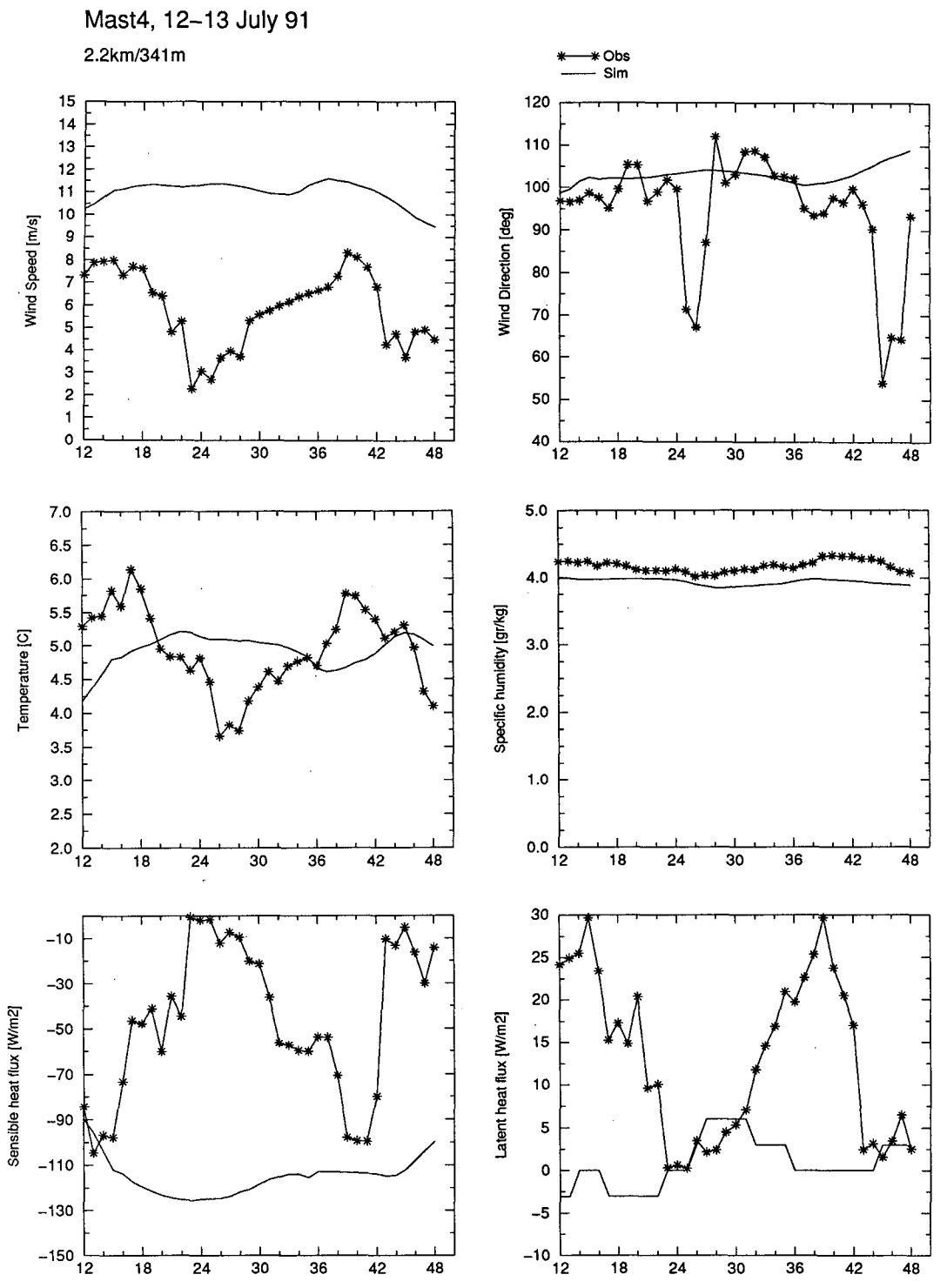

FIG. 13. Comparison between observations and simulation 1, for mast 4 (located on the ice sheet, 2.2 km from the ice sheet margin): (1) top left panel: wind speed 6 m above the surface (in m s^{-1}); (2) top right panel: wind direction (in degrees); (3) middle left panel: temperature 2 m above the surface (in K); (4) middle right panel: air specific humidity 2 m above the surface (in g kg^{-1}); (5) bottom left panel: sensible heat flux (in W m^{-2}—positive upward); (6) bottom right panel: latent heat flux (in W m^{-2}—positive upward). The observations are represented by the stars.

representation of the tundra topography (and consequently of the ice sheet margin slope) than to the tundra heating.

b. *Sensitivity to the large-scale wind forcing*

We will now discuss the MAR sensitivity to the synoptic-scale wind forcing. Two experiments will illustrate it. They differ from the standard experiment as follows: in experiment 3, the constant potential vorticity constraint is not used in the wind initialization; only the mass flux is prescribed to be $p_{*L}u_L = p_{*,0}u_{L,0}$, where $p_{*,0}$ and $u_{L,0}$ are taken from the sounding; moreover the geostrophic wind is taken as $(u_g, v_g) = (u_{L,0}, v_{L,0})$; in experiment 4, the synoptic-scale forcing has been reset to zero, and the model is initialized from a state at rest. The results of these experiments are summarized in Table 3. They show a significant sensitivity to the synoptic-scale forcing. When the initialization procedure is not based on the potential vorticity conservation in the large-scale flow, the model tends to overestimate the katabatic wind, especially the second day. This is simply due to the fact that the potential vorticity conservation, which is also contained in the full model equations, is such that the y wind component is increased from the ice sheet top to reach a spurious high value over the ice sheet slope. Moreover, because of the too large y wind component, the turbulent heat exchanges with the surface are increased. A spurious cooling of the upper part of the katabatic layer results, increasing the katabatic force. Consequently, the height of the katabatic layer and the downslope wind component also increase spuriously. It may be seen in Table 3 that at mast 9 the wind increases significantly when compared to that simulated in the standard. Moreover, the model seems to diverge: after 48 simulated hours at mast 9, for example, experiment 3 overestimates the wind speed by 80% (spurious wind speed increase from 5.2 m s^{-1} to 9.2 m s^{-1}) and the downward sensible heat flux by 100%. The height of the wind speed maximum is also doubled.

When a zero synoptic-scale forcing is prescribed (experiment 4), it is found (see Table 3) that the wind speed over the ice sheet is smaller than in the standard. When compared to the observations, it is overestimated at mast 4, especially at night. Nevertheless at mast 9, it is underestimated by up to 15% (at 1500 LT). In experiment 4, the simulated temperatures are lower than in the standard and slightly underestimated when compared to the observations. The wind speed at mast 6 (not shown) is smaller by 2 m s^{-1} as compared to the observations and the standard. Temperature at the same mast is underestimated at night by 1.5°C, whereas it is overestimated by 1.1°C in the standard, when compared to the observations. In fact, experiment 4 gives acceptable results when considering the observations near the surface. Nevertheless, in experiment 4 the thickness of the katabatic layer is 40 m at night—that is, two times smaller than in the standard and observations—and the simulated wind speed is almost zero at 80 m above the surface.

One may characterize the model sensitivity to the synoptic-scale forcing used by analyzing the impact on the snow/ice melting. This is shown in Fig. 14 for the second day of integration (13 July). Differences are large, and may amount to no less than 25% in the area of mast 6, when the synoptic-scale forcing is not taken into account. This suggests that the katabatic circulation is strongly influenced by the synoptic-scale forcing. The main consequence for the surface energy balance is an increase of the katabatic flow efficiency in transferring heat to the ice sheet surface.

Finally, one has tested the model sensitivity to the presence of a hot tundra, when the synoptic-scale forcing is not included. This is done by comparing experiment 5 and experiment 6, which differs from experiment 5 by the fact that tundra is replaced by ocean. It is seen in Table 3 that the model sensitivity is much larger than that between experiments 1 and 2 (for which the synoptic-scale forcing is included). At mast 4 for example, the simulated temperature difference between experiments 5 and 6 amounts to 0.8°C, while it

TABLE 3. Summary of the sensitivity experiments along the GIMEX transect, 13 July. Observations (referred as OBS) are also indicated when available.

	Wind speed (m s^{-1})				Temperature (°C)						
	Mast 4		Mast 9		Mast 4		Mast 9		Snow/ice melting (cm WE)		
Expt.	0300 LT	1500 LT	0300 LT	1500 LT	0300 LT	1500 LT	0300 LT	1500 LT	Mast 4	Mast 6	Mast 9
OBS	4.0	8.3	5.5	4.6	3.8	5.8	−2.0	1.2	4.8		
STD	8.1	9.7	6.9	5.0	4.7	4.5	−2.6	1.9	4.8	5.6	1.6
1	11.3	11.4	6.8	5.0	5.0	4.7	−2.5	1.8	5.6	5.5	1.6
2	10.3	9.5	6.8	5.0	5.3	4.7	−2.5	1.8	5.3	5.5	1.6
3	8.9	10.2	9.1	7.4	5.4	5.7	1.0	3.0	5.5	6.4	2.2
4	7.4	8.2	5.2	3.9	3.5	4.0	−2.9	1.2	4.3	4.6	1.3
5	9.8	8.8	4.1	2.3	3.8	3.8	−4.0	1.0	4.6	4.6	1.3
6	6.3	4.2	4.0	1.8	3.0	3.0	−4.2	1.0	3.4	4.3	1.2

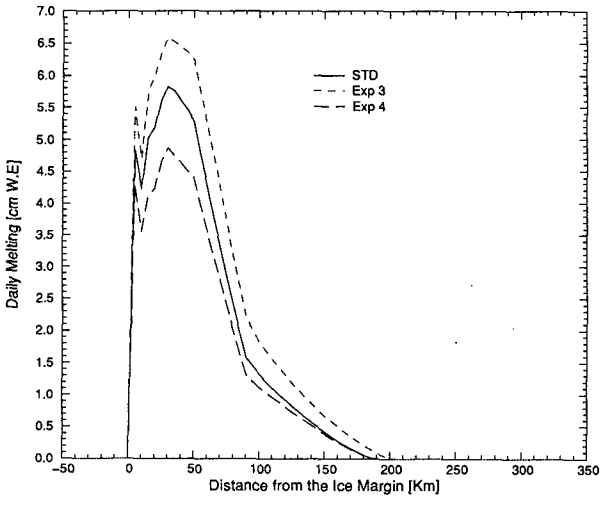

FIG. 14. Heat available for ice/snow melt (in cm WE day^{-1}), as a function of the distance to the ice sheet margin (in km), for the second simulated day (corresponding to 13 July 1991). Comparison between the standard and sensitivity experiments: solid line: standard; dashed line: experiment 3 (the initial cross-slope wind component is constant); axis line: experiment 4 (the synoptic-scale forcing is assumed to be zero).

only amounts up to 0.3°C between experiments 1 and 2. This reflects a lower impact of tundra heating at mast 4 when the geostrophic forcing is added. Snow/ice melting at masts 4 and 6 is also much less influenced by the tundra heating in this case. This suggests that even a weak easterly synoptic-scale forcing is strong enough to overwhelm significantly the contribution of the snow-free tundra heating to the snow/ice melting over the ablation zone.

6. Conclusions

In order to study the physical processes governing the ice/snow melting, the two-dimensional version of a meso-γ-scale atmospheric model MAR has been used to simulate the atmospheric circulation near the margin of the west Greenland ice sheet. The simulations shown here are two-dimensional, and cover the 12–13 July 1991 period. Simulated wind, temperature, and turbulent fluxes compare generally well with available observations, especially further above the ice sheet. The agreement is not so good just near the ice sheet margin (i.e., at mast 4), but this could be due to the crude representation of the tundra topography and the ice sheet margin slope.

Model sensitivity to the synoptic-scale wind forcing is significant. A simple initialization scheme, based on the potential vorticity conservation of the synoptic-scale flow, has been developed. It considerably improves the simulation. Finally, it is found that easterly synoptic-scale forcing influences the katabatic circulation. Even a weak easterly flow, which prevailed during the 12–13 July 1991 period and often occurs in this region of Greenland, overwhelms significantly the impact of a hot tundra on the ice sheet melting, so that the Greenland ice sheet mass balance for situations similar to that of the 12–13 July 1991 period is not significantly sensitive to the influence of a hot tundra.

Such study suggests the potential of mesoscale models when studying the impact of climatic changes over the ice sheets. Indeed, climate signals are transferred to the ice by the atmospheric boundary layer. Using a mesoscale model like this is a first step toward bridging the gap between atmospheric and mass balance models. Moreover, mesoscale models like this could be used to test bulk models of the ABL that can be applied to the entire Greenland ice sheet.

Acknowledgments. This research is sponsored by the Climate Programme of the Commission of the European Communities under Grants EV5V-CT92-0132. H. Gallée is supported by the Belgian Scientific Research Program on the Antarctic of the Prime Minister's Science Policy Office. M. R. van den Broeke receives funding from the Dutch National Research Programme on Global Air Pollution and Climate Change (Contract 276/91-1200). The authors wish to thank the constructive comments made by the two anonymous reviewers, and Dr. G. Schayes, Dr. P. G. Duynkerke, and Prof. J. Oerlemans for thoughtful discussions. The model was run within the scope of a study contract between IBM of Belgium s.a. and the Université Catholique de Louvain, allowing the use of an IBM RS/6000 workstation.

APPENDIX

Model Initialization

To take into account in a simple way the synoptic-scale wind forcing over an ice sheet, a simple initialization procedure is presented here, based on the potential vorticity conservation of the flow. The synoptic-scale flow (u_L, v_L) is assumed to be barotropic. Vertical motion relative to σ surfaces is neglected.

For such flow, the MAR equations reduce to

$$\frac{\partial u_L}{\partial t} + u_L \frac{\partial u_L}{\partial x} + v_L \frac{\partial u_L}{\partial y} = -\left.\frac{\partial \phi_g}{\partial x}\right|_p + f v_L \quad \text{(A1)}$$

$$\frac{\partial v_L}{\partial t} + u_L \frac{\partial v_L}{\partial x} + v_L \frac{\partial v_L}{\partial y} = -\left.\frac{\partial \phi_g}{\partial y}\right|_p - f u_L \quad \text{(A2)}$$

$$\frac{\partial p_{*L}}{\partial t} + \frac{\partial (p_{*L} u_L)}{\partial x} + \frac{\partial (p_{*L} v_L)}{\partial y} = 0, \quad \text{(A3)}$$

in which $(\partial\phi_g/\partial x|_p, \partial\phi_g/\partial y|_p) = (fv_g, -fu_g)$ is the synoptic-scale pressure gradient force. Note that in our model the initial mean sea level pressure $p_s = p_{sL}$ is assumed to be constant (Gallée and Schayes 1994). We further assume that the synoptic-scale pressure thickness $p_{*L} = p_{sL} - p_t$ is stationary.

Defining $\zeta_L = \partial v_L/\partial x - \partial u_L/\partial y$, it is easily found that the following quantity is conserved:

$$E = \frac{\zeta_L + f}{p_{*L}}.$$

It represents the potential vorticity of the synoptic-scale flow.

Even when the homogeneity along the y axis is assumed, E is conserved. In this case, $\zeta_L = \partial v_L/\partial x$, and the mass flux is $p_{*L}u_L$.

The initialization of the two-dimensional model version is performed by keeping $p_{*L}u_L$ = constant and E = constant. One proceeds as follows:

1. Using the mass conservation constraint $p_{*L}u_L$ = constant, computes u_L at every grid point from its value at the grid point corresponding to the sounding.
2. Using the potential vorticity conservation constraint E = constant, computes v_L at every grid point. In the present study, one takes $\zeta_L = 0$ at the grid point corresponding to the sounding.
3. Using the momentum equation (A2) in the y direction, computes u_g from the local values of ζ_L and u_L.
4. Using the momentum equation (A1) in the x direction, computes v_g from the local values of ζ_L, u_L, and v_L.

REFERENCES

Ambach, W., 1977a: Untersuchungen zum Energieumsatz in der Ablationszone des Grönländische Inlandeises. *Expedition Glaciologique Internationale au Groenland* 4, No. 5, Bianco Lunos Bogtrykkeri A/S, Kobenhavn, 63 pp.

——, 1977b: Untersuchungen zum Energieumsatz in der Akkumulationszone des Grönländische Inlandeises. *Expedition Glaciologique Internationale au Groenland* 4, No. 7, Bianco Lunos Bogtrykkeri A/S, Kobenhavn, 44 pp.

——, 1985: Characteristics of the heat balance of the Greenland Ice Sheet for modelling. *J. Glaciol.*, **31,** 3–12.

Anthes, R. A., Y.-H. Kuo, E.-Y. Hsie, S. Low-Nam, and T. W. Bettge, 1989: Estimation of skill and uncertainty in regional numerical models. *Quart. J. Roy. Meteor. Soc.*, **115,** 763–806.

Deardorff, J. W., 1978: Efficient prediction of ground surface temperature and moisture with inclusion of a layer of vegetation. *J. Geophys. Res.*, **83,** 1889–1903.

Duynkerke, P. G., 1988: Application of the E-ϵ turbulence closure model to the neutral and stable atmospheric boundary layer. *J. Atmos. Sci.*, **45,** 865–880.

——, 1991: Radiation fog: A comparison of model simulation with detailed observations. *Mon. Wea. Rev.*, **119,** 324–341.

——, and M. R. van den Broeke, 1994: Surface energy balance and katabatic flow over glacier and tundra during GIMEX-91. *Global Planetary Change,* **9,** 17–28.

Gallée, H., and G. Schayes, 1992: Dynamical aspects of katabatic winds evolution in the Antarctic Coastal Zone. *Bound.-Layer Meteor.*, **59,** 141–161.

——, and ——, 1994: Development of a three-dimensional meso-γ primitive equations model, katabatic winds simulation in the area of Terra Nova Bay, Antarctica. *Mon. Wea. Rev.*, **122,** 671–685.

——, J. P. van Ypersele, I. Marsiat, T. Fichefet, C. Tricot, and A. Berger, 1992: Simulation of the last glacial cycle by a coupled 2-D climate-ice sheet model. Part 2: Response to insolation and CO_2 variation. *J. Geophys. Res.*, **97,** 15 713–15 740.

——, ——, and A. Berger, 1993: Development of a three-dimensional meso-γ primitive equations model, katabatic winds simulation in the area of Terra Nova Bay, Antarctica. *Belgian Scientific Research Programme on the Antarctic, Scientific Results of Phase Two (November 1988–May 1992),* Vol. 3, S. Caschetto, Ed., Prime Minister's Services, Science Policy Office, II/03-1–II/03-36.

Huybrechts, P., A. Letréguilly, and N. Reeh, 1991: The Greenland ice sheet and greenhouse warming. *Palaeogeogr., Palaeoclimatol., Palaeoecol. (Global Planetary Change),* **89,** 399–412.

Kodama, Y., G. Wendler, and N. Ishikawa, 1989: The diurnal variation of the boundary layer in summer in Adélie Land, Eastern Antarctica. *J. Appl. Meteor.*, **28,** 16–24.

Letréguilly, A., N. Reeh, and P. Huybrechts, 1991: The Greenland ice sheet through the last glacial-interglacial cycle. *Palaeogeogr., Palaeoclimatol., Palaeoecol. (Global Planetary Change),* **90,** 385–394.

Lliboutry, L., 1965: *Traité de Glaciologie.* Masson, 1040 pp.

Mahrt, L., 1982: Momentum balance of gravity flows. *J. Atmos. Sci.*, **39,** 2701–2711.

Meesters, A. G. C. A., E. A. C. Henneken, N. J. Bink, H. F. Vugts, and F. Cannemeijer, 1994: Simulation of the atmospheric circulation near the Greenland ice sheet margin. *Global Planetary Change,* **9,** 53–68.

Murphy, B. F., and I. Simmonds, 1993: An analysis of strong wind events simulated in a GCM near Casey in the Antarctic. *Mon. Wea. Rev.*, **121,** 522–534.

Oerlemans, J., 1991: The mass balance of the Greenland ice sheet: Sensitivity to climate change as revealed by energy-balance modelling. *Holocene,* **1,** 40–49.

——, and C. J. van der Veen, 1984: *Ice Sheets and Climate.* D. Reidel Publishing Company, 217 pp.

——, and H. F. Vugts, 1993: A meteorological experiment in the melting zone of the Greenland Ice Sheet. *Bull. Amer. Meteor. Soc.*, **74,** 355–365.

Ohmura, A., 1987: New temperature distribution maps for Greenland. *Z. Gletscherkd. Glazialgeol.*, **23,** 1–45.

——, and team members, 1992: ETH Greenland Expedition, Progress Report No. 2. April 1991 to October 1992, Department of Geography ETH, Zurich, 94 pp.

Pettré, P., and J. C. André, 1991: Surface-pressure change through Loewe's phenomena and katabatic flow jumps: Study of two cases in Adélie Land, Antarctica. *J. Atmos. Sci.*, **48,** 557–571.

Stull, R. B., 1993: *An Introduction to Boundary Layer Meteorology.* Kluwer Academic Publishers, 666 pp.

Van de Wal, R. S. W., and A. J. Russell, 1994: A comparison of energy balance calculations, measured ablation and meltwater runoff near Søndre Strømf jord, West Greenland. *Global Planetary Change,* **9,** 29–38.

van den Broeke, M. R., P. G. Duynkerke, and J. Oerlemans, 1994: The observed katabatic flow at the edge of the Greenland ice sheet during GIMEX-91. *Global Planetary Change,* **9,** 3–15.

Yen, Y.-C., 1981: Review of thermal properties of snow, ice and sea ice. *CRREL Rep.*, 81-10.